# A High-Resolution Modeling Study of the 24 May 2002 Dryline Case during IHOP. Part II: Horizontal Convective Rolls and Convective Initiation

MING XUE

*School of Meteorology, and Center for Analysis and Prediction of Storms, University of Oklahoma, Norman, Oklahoma*

WILLIAM J. MARTIN

*Center for Analysis and Prediction of Storms, University of Oklahoma, Norman, Oklahoma*

(Manuscript received 8 November 2004, in final form 21 June 2005)

ABSTRACT

In Part I of this paper, the timing and location of convective initiation along a dryline on 24 May 2002 were accurately predicted, using a large 1-km-resolution nested grid. A detailed analysis of the convective initiation processes, which involve the interaction of the dryline with horizontal convective rolls, is presented here.

Horizontal convective rolls (HCRs) with aspect ratios (the ratio of roll spacing to depth) between 3 and 7 develop in the model on both sides of the dryline, with those on the west side being more intense and their updrafts reaching several meters per second. The main HCRs that interact with the primary dryline convergence boundary (PDCB) are those from the west side, and they are aligned at an acute angle with the dryline. They intercept the PDCB and create strong moisture convergence bands at the surface and force the PDCB into a wavy pattern. The downdrafts of HCRs and the associated surface divergence play an important role in creating localized maxima of surface convergence that trigger convection. The downward transport of westerly, southwesterly, or northwesterly momentum by the HCR downdrafts creates asymmetric surface divergence patterns that modulate the exact location of maximum convergence. Most of the HCRs have a partially cellular structure at their mature stage. The surface divergence flows help concentrate the background vertical vorticity and the vorticity created by tilting of environmental horizontal vorticity into vortex centers or misocyclones, and such concentration is often further helped by cross-boundary shear instability. The misocyclones, however, do not in general collocate with the maximum updrafts and, therefore, the points of convective initiation, but can help enhance surface convergence to their south and north.

Sequences of convective cells develop at the locations of persistent maximum surface convergence, then move away from the source with the midlevel winds. When the initial clouds propagate along the convergence bands that trigger them, they grow faster and become more intense. While the mesoscale convergence of dryline circulation preconditions the boundary layer by deepening the mixed layer and lifting moist air parcels to their LCL, it is the localized forcing by the HCR circulation that determines the exact locations of convective initiation. A conceptual model summarizing the findings is proposed.

## 1. Introduction

The dryline is frequently observed in the western Great Plains of the United States, usually as a boundary between warm, moist air from the Gulf of Mexico, and hot, dry continental air from the semiarid southwestern states or the Mexican plateau. The dryline is often the focus of convection initiation (CI) (Rhea 1966). Despite a number of existing studies (Bluestein and Parker 1993; Ziegler and Hane 1993; Ziegler et al. 1995; Shaw et al. 1997; Atkins et al. 1998; Ziegler and Rasmussen 1998; Hane et al. 2002; Peckham et al. 2004), the exact processes by which convection is initiated are still not well understood (Hane et al. 1993). The exact timing and location that convection is initiated along drylines are even harder to predict.

In most cases, initiation of deep convection along the drylines occurs at isolated locations instead of as a band of convection along the entire dryline. Observational

*Corresponding author address:* Dr. Ming Xue, School of Meteorology, University of Oklahoma, 100 E. Boyd, Norman, OK 73019.
E-mail: mxue@ou.edu

studies have identified several mechanisms potentially responsible for creating preferred locations for CI along the dryline or other types of low-level convergence boundaries. They include the enhancement of vertical lifting through the interaction of boundary layer horizontal convective rolls (HCRs) with the dryline (Atkins et al. 1998), the development of Kelvin–Helmholtz instability due to cross-line shear [KHI; e.g., Mueller and Carbone (1987); Lee and Wilhelmson (1997) for outflow boundary; Rao and Fuelberg (2000) for sea-breeze boundary], misocyclones (e.g., Wilson et al. 1992; Buban et al. 2003; Richardson et al. 2003; Murphey et al. 2006), and surface heat flux gradients due to heterogeneous land surface properties (Hane et al. 1997).

Atkins et al. (1998) showed clear examples of HCRs in the environment of a dryline using Weather Surveillance Radar-1988 Doppler (WSR-88D) and airborne Doppler radar data. These data revealed dryline variability in the horizontal along-line direction that was created as the dryline interacted with HCRs forming west of the dryline. The rolls intersected the dryline at periodic locations creating radar reflectivity and vertical velocity maxima and, more importantly, initiated clouds at these intersection points. Hane et al. (2001) observed two thin lines immediately to the west of a dryline and suggested that they were due to HCRs. For the case investigated in this study, Wakimoto et al. (2006) point to the presence of cellular structures in the reflectivity field seen by an airborne radar flown at 600 m AGL, during the hour preceding CI. A wavy pattern of thin lines is reported by them and is suggested to be the result of HCRs interacting with the dryline. Hane and Richter (2004) summarize a series of case studies that emphasize the importance of processes that occur in the dry air in creating increased low-level convergence in local areas along the dryline leading to convective initiation.

Wilson et al. (1992) performed a detailed study on the initiation of thunderstorms along a quasi-stationary convergence boundary associated with the so-called Denver cyclone (Crook et al. 1991) using both special observational data and data from model simulations. Misocyclones, defined as vertical vortices of less than 4 km in diameter by Fujita (1981), were found in the observations to form periodically along the main convergence line, and initial clouds that formed south of the misocyclones were found to intensify as they move over the misocyclones, which were believed to contain enhanced upward motion. The observed misocyclones and clouds tended to drift apart after they crossed each other, however. One finding of this study is that the initial clouds did not seem to form over the misocyclones despite the enhanced updraft they were believed to contain. Their numerical simulations suggested that the vertical vorticity in the misocyclone came from the horizontal shear, which was intensified mainly by stretching that is associated with locally enhanced updraft created by the HCRs intersecting the dryline. A question that remains, however, is why convection was not initiated at the misocyclone locations if they indeed contained the vertical velocity maxima on the convergence line. Also, in their simulation, the observed southwesterly flow west of the dryline was simulated as from the northwest instead; the implication of this on the misocyclone development and the role of misocyclones in convective initiation is unclear. Still, the important role of the interaction of HCRs with the convergence line is evident.

Murphey et al. (2006) analyzed the thin structure and convective initiation along the dryline of 19 June 2002, a case from the 2002 International $H_2O$ Project (IHOP_2002; Weckwerth et al. 2004) field experiment. Data from airborne Doppler radar and water vapor differential absorption lidar (DIAL) were used. In that case, the along-line variability found in the data was attributed to numerous misocyclones that distorted the thin line and the misocyclones influenced the locations of the updraft with most of the peak values positioned north of the circulations. These updrafts coincided with the triggering of initial convective cells. The HCRs, at least those east of the dryline, were found to be parallel to the line and, therefore, would not explain the localized enhancement of vertical motion or the formation of misocyclones. KHI was believed to be the cause of those misocyclones. Further, the misocyclones were found to contain a downdraft core at their center, due to a dynamically induced downward pressure gradient force (Klemp and Rotunno 1983; Lee and Wilhelmson 1997); therefore these misocyclones were generally not collocated with the updrafts and hence did not trigger convection.

During IHOP_2002, a dryline formed on 24 May and intense convection was initiated along the line in the afternoon. The event was intensively observed during the field experiment for the purpose of studying CI and possible interaction of the dryline with an intersecting cold front (Weckwerth et al. 2004). A rich set of special observations was collected during the field experiment and additional data were gathered in post–real time from various networks of surface stations (Weckwerth et al. 2004). For this reason, the case has been studied by a number of researchers (e.g., Geerts et al. 2006; Holt et al. 2006; Wakimoto et al. 2006) from different perspectives.

In the first part of this paper (Xue and Martin 2006, referred to hereafter as Part I), a successful simulation

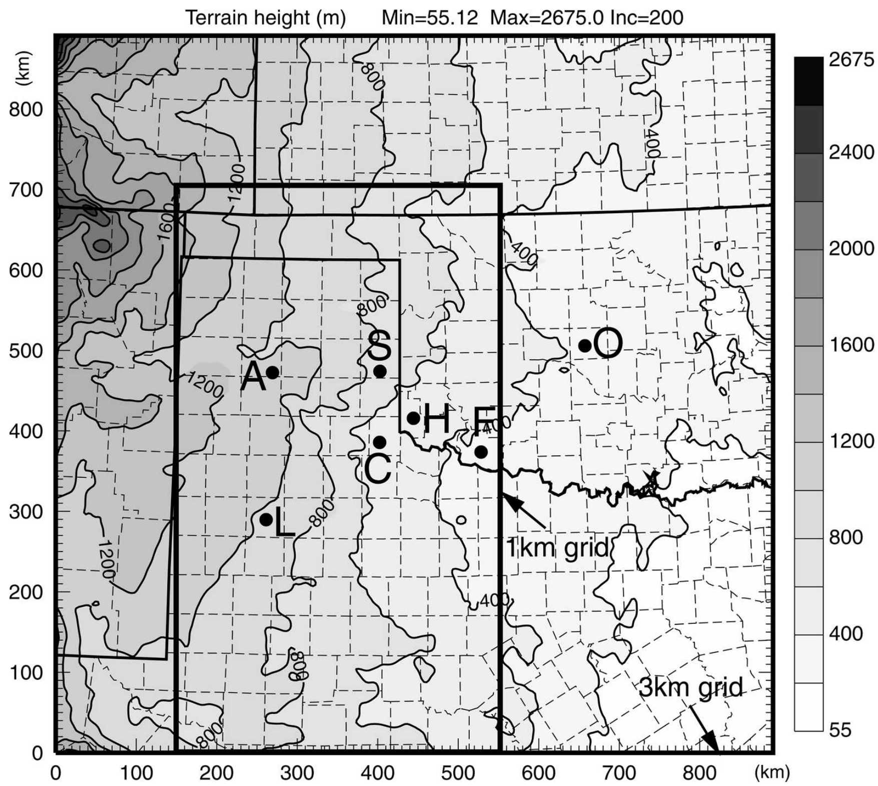


FIG. 1. The 3-km model domain with shaded terrain elevation contours. The nested 1-km domain is indicated by the rectangular box, which used a separate higher-resolution terrain definition. The 1-km grid shares the south boundary with the 3-km one. Letters A, L, S, C, H, F, and O in the figure indicate the locations of Amarillo, Lubbock, Shamrock, and Childress in Texas, and Hollis, Frederick, and Oklahoma City in Oklahoma. Also shown are county and state boundaries.

of the 24 May 2002 case is described. The nonhydrostatic Advanced Regional Prediction System (ARPS) model (Xue et al. 2000, 2003) is used to simulate the evolution of the dryline and the intersecting cold front as well as the initiation and development of convective storms along and near the dryline and cold front. Using a large (700 km × 400 km) 1-km horizontal resolution grid nested within an even larger 3-km grid (Fig. 1), the model is able to accurately predict the evolution of the dryline, the development and evolution of realistic boundary layer convective eddies and horizontal rolls, and most importantly, the timing and location of convective initiation along a section of dryline in western Texas. The model predicted the timing and location of convective initiation accurate to within 20 min and 25 km, respectively.

In Part I, it is suggested that the interaction between the dryline and the horizontal convective rolls from the west side of the dryline play an important role in determining the preferred locations of convective initiation along the dryline. Such interaction creates localized maximum surface convergence that provides additional forcing to lift air parcels above their level of free convection (LFC). The mesoscale convergence in the dryline zone and the resultant upward bulging of the well-mixed moist boundary layer created a favorable zone for moist convection.

In this paper, the development and evolution of the boundary layer (BL) HCRs and open convective cells (OCCs) and their interaction with the dryline are analyzed in detail in section 2. The processes by which a series of (moist) convective cells are triggered are discussed in section 3. The possible role of misocyclone vortices that form along the main convergence line is also discussed. In section 4, we propose a conceptual model that summarizes our findings. A summary is then given in section 5.

## 2. The development and evolution of HCRs preceding CI

The studies based on observational data, cited in the introduction, though very valuable, are usually subject to the limitations of data coverage in both space and time. Only a few numerical simulation studies on the interaction of HCRs with a dryline in the context of CI exist (Ziegler et al. 1997; Richter and Hane 2003; Peckham et al. 2004), and they either used relatively coarse resolutions or idealized conditions. The current understanding of the convective initiation processes along drylines remains incomplete. In the high-resolution (1 km) simulation study of Peckham et al. (2004) that employs idealized terrain, sounding, and periodic north–south boundary conditions, HCRs and OCCs were found to develop on both sides of the dryline, with those on the west side having deeper and stronger vertical circulations. The OCCs and HCRs east of the dryline were found to impact the dryline and convective cloud location by modulating the low-level moisture and upslope easterly flow. The interaction between OCC and HCR circulations and the dryline appeared primarily responsible for creating a considerable amount of along-line variation in the dryline characteristics. Many shallow convective clouds developed along and west of the dryline over the OCC and HCR updrafts as well as OCC–dryline and HCR–dryline intersection points, and they evolved into deep convective clouds where OCCs and HCRs to the east intersect the dryline near the same location. While many of the results of the study appear realistic, it is limited by its use of idealized conditions, the most restrictive of which being perhaps the periodic north–south boundary conditions. A preliminary real-case modeling study of Richter and Hane (2003) did involve the development of HCRs and their interaction with the dryline. Their study emphasizes the role of the so-called clear air downdrafts, forming as part of the downward branches of HCRs in the dry air that intersect the dryline at an angle. Such downdrafts are believed to carry large westerly momentum to low levels thereby enhancing the low-level convergence locally. The study of Ziegler et al. (1997) also pointed out the presence of HCRs in their numerical simulations although it did not carefully examine or emphasize their possible role in CI. A close examination of their figures (e.g., Fig. 6a) does suggest local enhancement of surface convergence and vertical motion at the intersecting points.

In Part I, it is pointed out that boundary layer convective eddies and horizontal rolls quickly develop after the model initial time in our simulation. Active dry convection spans a width of 100 to 150 km on both sides of the dryline south of the cold front by 2000 UTC (hereafter all times are UTC), that is, 2 h into the forecast, and such eddies and rolls are also evident in the radar reflectivity observations. The convective eddies and rolls are believed to be processes through which the vertical mixing and deepening of the convective boundary layers on both sides of the dryline are realized. Further, it is also noted that the boundary layer convective eddies and rolls, mainly those on the west side of the dryline, are responsible for creating locally enhanced convergence at the surface that appears to be responsible for CI at specific locations along the dryline. In this section, we analyze the evolution of HCRs preceding the dryline CI in more detail. We note here that the HCRs we refer to in this study are usually not purely two-dimensional rolls; significant along-roll variability often exists and sometimes the rolls appear more like elongated OCCs. We refer to them as rolls as long they do not appear circular in shape.

The evolution of the HCRs in the 1.5-h period preceding CI is illustrated in Fig. 2, which shows the near-surface moisture convergence fields. The figure centers around the SSW–NNE-oriented primary dryline convergence boundary (PDCB) and corresponds to the west portion of the domain shown in Fig. 9 of Part I. Here we define the PDCB as the strong mesoscale convergence zone or boundary between the generally southeasterly flow on the east side and generally westerly flows on the west side of the dryline. This boundary is usually located near the eastern edge of the zone of strong surface moisture gradient that often spans a width of 50 to 100 km (see, e.g., Fig. 3 of Part I) while the PDCB is much narrower.

By 1830, 30 min after the initial time of the 1-km forecast, bands of enhanced surface convergence due to HCRs [roll convergence bands (RCBs)] have developed along the PDCB (Fig. 2a) and these bands are labeled R0 through R5. RCBs R1, R3, and R5 are responsible for the later triggering of three groups of convective cells along the PDCB in the model. The spacing between the RCBs ranges from 40 to 80 km and the southern ones are shorter and more distantly spaced. The convective eddies farther west of these bands show more open-cell structures. At this time, the positive vertical vorticity is generally collocated with positive convergence bands and the PDCB roughly collocates with the 10 g kg$^{-1}$ $q_v$ contour. At 1900 (Fig. 2b), more roll structures are established to the west of the original ones, with the latter becoming longer, narrower, and more intense; the $q_v$ convergence maximum is more than doubled from 1830. The PDCB and the leading RCBs have progressed eastward by about 80 km. The RCB labeled R1 remains the strongest and all convergence bands appear collocated with the bands of positive vorticity.

In general, the negative vorticity bands are much weaker than the positive bands, reflecting the positivity of the background or mesoscale vertical vorticity in the

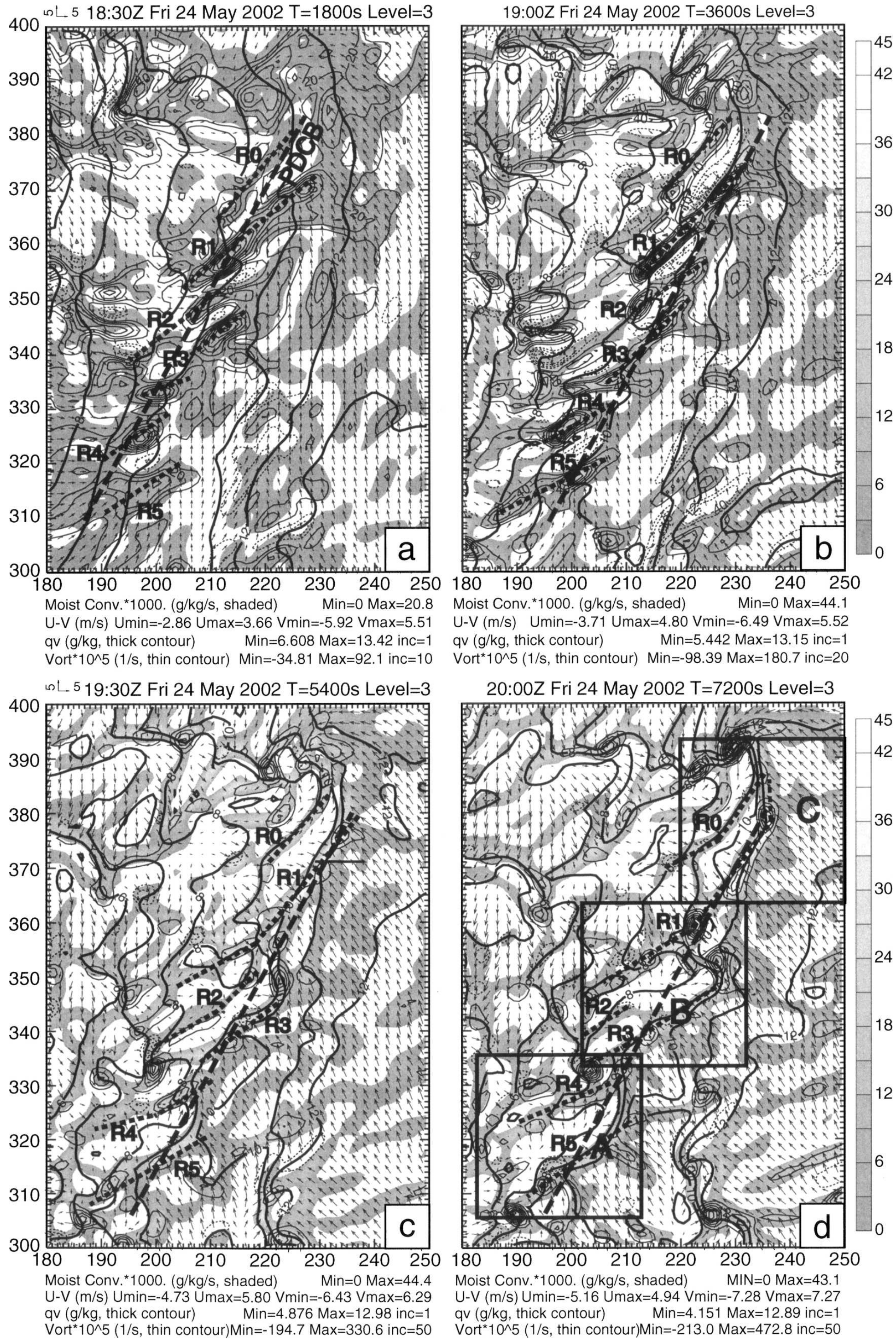


FIG. 2. Model-simulated near-surface (about 30 m AGL) moisture convergence fields (gray shading, values amplified by a factor of 1000, and only positive values shown), the horizontal wind vectors [vector key shown at the top left of (a) and (c) plots, m s$^{-1}$], the water vapor mixing ratio, $q_v$, field (thick contours), and the vertical vorticity (thin black contours, amplified by a factor of $10^5$), at (a) 1830, (b) 1900, (c) 1930, and (d) 2000 UTC 24 May 2002. No reflectivity exists at these times. The thick long-dashed line drawn in each panel indicates the location and orientation of the PDCB as labeled in (a) between the moist air mass to its east and the dry air mass to its west. The thick short-dashed lines in each panel mark the positions of HCR convergence bands near the PDCB and are labeled R0 through R5. Maximum and minimum values and contour intervals are indicated in the figure. The fields were smoothed once using a nine-point filter before plotting. Model level 3 is about 30 m AGL. The initial locations of convective storms initiated at around 2204, 2015, and 2027 UTC in the model are marked by A, B, and C in (d). The three square boxes in (d) indicate the subdomains to be shown in Fig. 3.

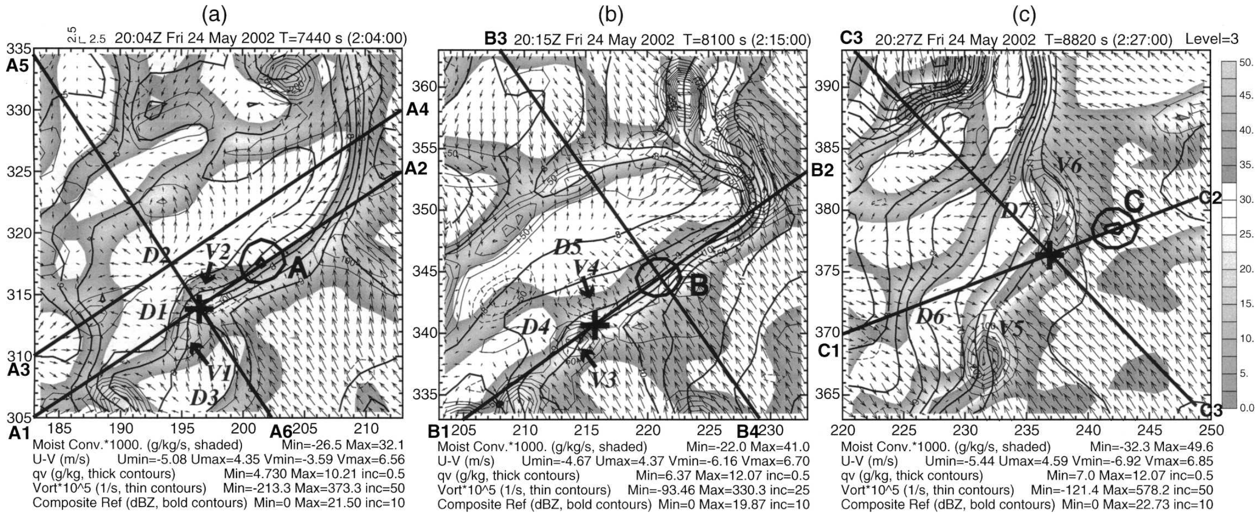


FIG. 3. As in Fig. 2 but for zoomed-in regions indicated by dashed square boxes in Fig. 2d. They are roughly centered on storm cells A, B, and C, respectively, near the time of their first echoes. Thick straight lines indicate locations of vertical cross sections to be shown in Figs. 4–10. Plus signs, "+," indicate the centers of maximum surface moisture convergence that trigger cells A, B, and C. Italic *D1–D7* are the centers of divergence associated with the OCCs. Italic *V1–V6* indicate (some through arrows) centers of maximum vorticity.

dryline zone, where the flow transitions from westerlies to southerlies. The horizontal convergence is responsible for most of the positive vorticity concentration along the convergence bands, and the weaker negative vorticity is believed to be created by the tilting of environmental horizontal vorticity. The latter is supported by the fact that at earlier stages of roll development, the negative vorticity generally lies on the left (looking downshear, which is also the direction of convergence bands) side of the RCBs where $w$ is at a maximum. The tilting of horizontal vorticity associated with the roll circulations has been proposed as a source of vertical vorticity in the literature (see, e.g., discussion in Murphey et al. 2006), but since the roll updrafts have little correlation with the horizontal vorticity maxima of the rolls, and the latter are weak initially, we discount this as the main source of vertical vorticity, as did Murphey et al. (2006) based on observational data.

By 1930 (Fig. 2c), even though the moisture convergence maximum remains at about the same value as at 1900, the average intensity of other bands has increased significantly as many of the bands west of the PDCB now show lighter shades. The elongated OCC structure now dominates the region right behind the leading HCRs (those close to the PDCB). Within these OCCs, divergence flow patterns are very clear. The transition toward the OCC structure indicates the increase of convective instability (Agee et al. 1973; Weckwerth et al. 1997; Kristovich et al. 1999) due to surface heating. A more wavy pattern has developed along the PDCB, with R1, R3, and R5 protruding into the moist air more than R0, R2, and R4, shifting the enhanced convergence regions somewhat northward along the former three bands. By this time, the vertical vorticity maxima have shifted mostly to the ends of these convergence bands and this becomes more prominent by 2000 (Fig. 2d).

While the initial establishment of the wavy pattern of the main convergence band is due to the HCR and PDCB interaction, the later concentration of vorticity toward the ends of the band and the further intensification of the rotation can be attributed to the process that is responsible for the shear instability or KHI that develops along a shear zone (see Batchelor 1967; Lee and Wilhelmson 1997). Within this process, the motion induced by the shear zone displacement advects the original shear zone vorticity toward the centers where the displacement is zero and increases the vorticity at these locations. The concentrated vorticity further amplifies the displacement, resulting in an instability with an exponential growth rate. This process is most typical with the RCB associated with cell C, as can be seen in Fig. 3c. The other bands are less typical because of the significant role of vorticity advection by the HCR divergent flows. When cumulus clouds move over these vorticity centers or misocyclones, nonsupercell tornadoes can develop due to vertical stretching (Wakimoto and Wilson 1989).

By 2000 (Fig. 2d), the OCC structure is further developed; most cells have now attained a near-circular shape with clearly defined divergent flow from the center. Even the leading HCRs have evolved into more elliptical shapes, and the northern portions of R2 and R4 are now eroded by, respectively, the divergence circulation between R3 and R1, and that between R5 and R3. Bands R5, R3, and R1 now dominate the impact on the shape of PDCB, and a major portion of R5 and R3 now extends ahead of the PDCB. Maximum convergence is now located right at the intercepting points of these bands with the PDCB, and these are also locations where the southeasterly winds from the moist side directly oppose the northwesterly winds originating from the centers of divergence located behind the RCBs. Three to four minutes after this time, the first radar echo exceeding 20 dB$Z$ appeared in the model (cf. Fig. 3a) centering on R5, and another 10 min or so later, another cell formed in a very similar way (cf. Fig. 3b) on R3. The initial locations of these first echoes are marked by A and B in Fig. 2d. At 2027, the first echo of the third cell group (location C in Fig. 2d) is observed in the model a few kilometers NW of the surface convergence maximum on R0. As will be seen more clearly later, the initiation of all three cells in the model is a result of the much enhanced surface convergence and vertical lifting associated with each of the three RCBs that intercept the PDCB. The initial observed cells, also three of them, formed at locations within 10 km of the model initiation points (see Fig. 8 of Part I), although the sequence is reversed in the model. The timing errors are about 15 min. In the observations, cell C was the strongest while in the model cells C and B were of similar intensity, at least later on (cf. Figs. 6, 8, 9 of Part I).

As pointed out in Part I, there is a vertical velocity maximum at 3 km AGL that is essentially over the low-level convergence maximum each time one of the cells is initiated. The radar echoes, after they form, generally propagate northeastward, in the direction of midlevel winds. These echoes appear anchored at the low-level initiation points and spread with time like a smoke plume. This behavior indicates sustained low-level lifting. In the next section, the connection of the storm initiation with the surface convergence maxima is examined in more detail using cross sections.

## 3. Initiation of convective cells

### a. Horizontal cross sections

Figure 3 shows an enlarged view of the areas indicated by the square boxes in Fig. 2d, with each roughly centering on cells A, B, and C at the time of their initiation. From Figs. 3a and 3b, we can see clearly that the surface divergence pattern to the NW of the cell-triggering convergence bands exhibits asymmetry; the northeastward flow is significantly stronger than the southwestward flow. The downward transport of southwesterly momentum is believed to be the main cause of this asymmetry. Figure 3c shows that the elliptically shaped HCRs NW of cell C exhibit a stronger northwesterly wind component, however. This is because this region is affected by the southeastward spreading cold air from the cold front, which can be seen more clearly in Fig. 2. At least partly for this reason, the HCBs near cell C are more parallel to the PDCB. The asymmetry of the divergent flow complicates the interaction of the HCR convergence bands with the PDCB.

In Fig. 3, the local maxima of moisture convergence along the main HCR bands are marked by "+." As we will see next, they represent the locations of maximum low-level forcing from which sequences of cells, including initial cells A, B, and C, are initiated. We will examine vertical cross sections through these maxima and/or through the center of initial cells.

### b. Vertical cross sections

Figure 4 shows vertical cross sections at 4-min intervals starting 8 min before the first reflectivity echo is observed (in the model) at 2004, through line A1–A2 in Fig. 3a. It can be seen that during this period, the maximum surface convergence (mainly due to opposing winds in the section-normal direction, although along-section convergence is also present) is located at 16 to 18 km along the horizontal axis (as indicated by vertically pointing single arrows; the origin is at A1). This strong convergence forces a vertical updraft of nearly 4 m s$^{-1}$ within the boundary layer, creating a local bump in the $q_v$ contours and producing a cloud in the 3–5-km layer at 1956 (Fig. 4a). Such bumps act as obstacles to faster flows above, forcing internal gravity waves that are seen as the periodic patterns in the horizontal moisture convergence fields (Fig. 4). While it is possible that these gravity waves, especially when they amplify, may interact with the boundary layer flow or even modulate the convection, we do not see any evidence of their doing so at this stage of development. By 2000 (Fig. 4b), the cloud has grown deeper, and there is an indication that the lifted air parcels have reached their LFC because they appear to be accelerating upward ($w$ increases with height). This is certainly true in the next few minutes as by 2004, the cloud top has reached 6.5 km and the first radar echo has appeared (Fig. 4c). Figure 4 also shows that clouds form in the model before 2000, matching very well with the satellite observations shown in Fig. 4 of Part I. Further, these clouds, after they form over the low-level convergence maximum, remain within this vertical cross section, or propagate along the HCR convergence band (Fig. 3a)

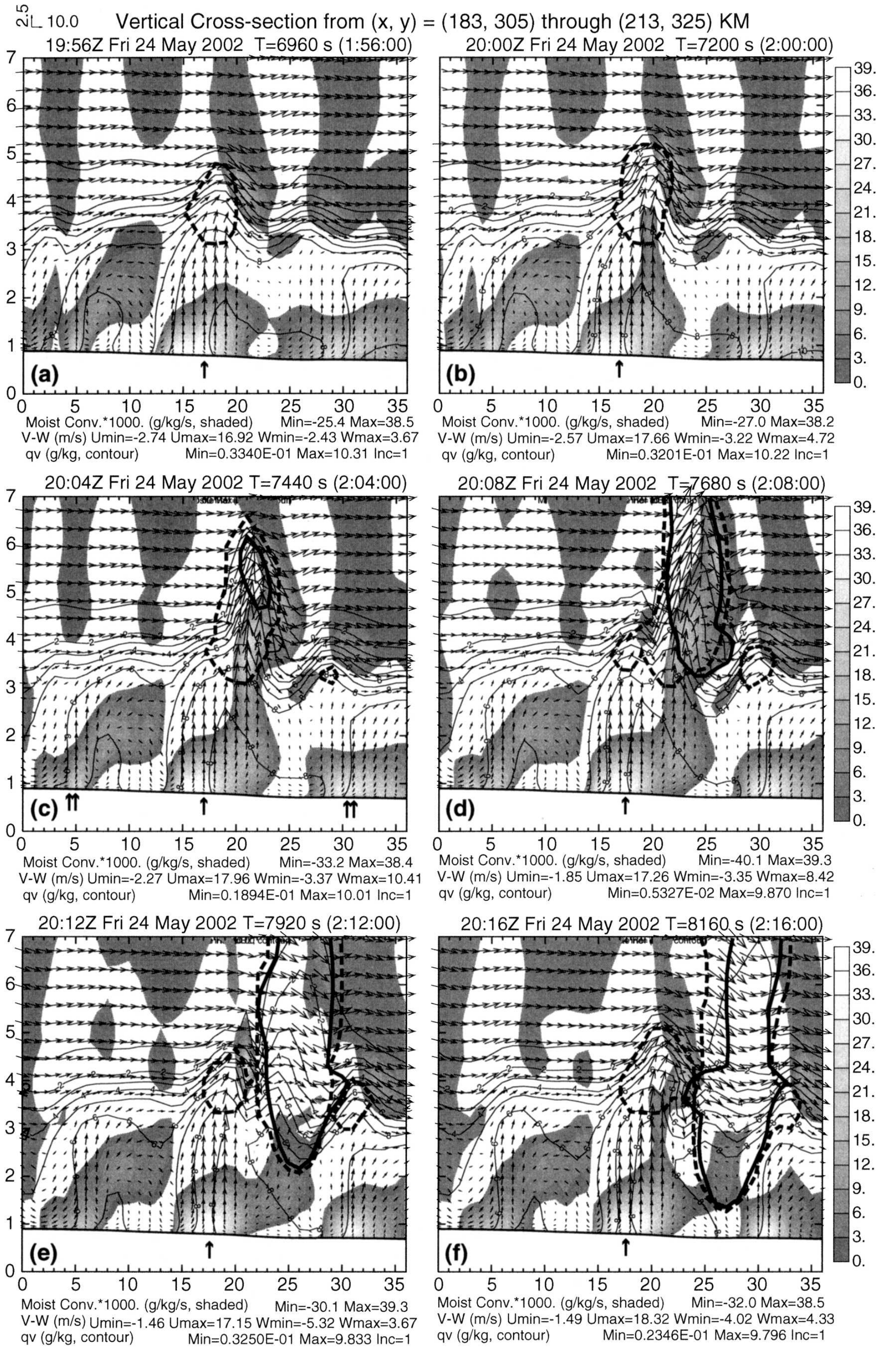


FIG. 4. Vertical cross sections along line A1–A2 in Fig. 3a at 4-min intervals starting from 1956 UTC 24 May 2002: $t$ = (a) 6960 s, (b) 7200 s, (c) 7440 s, (d) 7680 s, (e) 7920 s, and (f) 8160 s. Shown are the winds in the cross-section-parallel direction (vectors, m s$^{-1}$), the horizontal moisture convergence ($10^{-3}$ g kg$^{-1}$ s$^{-1}$, shaded), mixing ratio $q_v$ (thin contours, g kg$^{-1}$), the 0.01 g kg$^{-1}$ contour of total condensed water/ice outlining the cloud (thick dashed lines), and the 5-dB$Z$ reflectivity contour (thick solid lines). The upward pointing arrows below the ground level indicate locations of HCR convergence maxima, and double arrows in (c) indicate other maxima along the HCR band. The origin of the horizontal axes corresponds to A1 in Fig. 3a.

and, therefore, experience sustained upward forcing and quickly grow deeper.

At 2004, we note that a small cloud formed about 10 km downwind of the first cell, at the next "wave crest" in the $q_v$ contours. This crest is associated with the enhanced surface convergence about the same distance to the northeast of cell A (Fig. 3a). We see from Fig. 3 (also in Fig. 4c at double-arrowed locations) that there exists periodic enhancement of convergence *along* the HCR convergence bands, with intervals of 10 to 15 km. At these points, low-level along-cross-section convergence is evident. The cellular mode of boundary layer convection is most likely the cause of such periodic enhancement, while the internal gravity waves propagating above may also be responsible. However, that these convergence centers are quasi-stationary and the average wavelength of the gravity waves differs from the intervals of enhanced convergence argue against the latter. Several numerical and observational studies have examined the interaction between HCRs and gravity waves in the overlying stable atmosphere (e.g., Balaji and Clark 1988; LeMone 1990; Lane and Clark 2002). When the wave fronts are aligned with the rolls or the waves propagate perpendicular to the rolls, periodic enhancement of the roll updrafts can occur. This is not the true in the current case.

In the minutes that follow 2004, cell A (Fig. 4) grows in depth and continues to propagate northeastward, advected by prevailing winds in the cloud layer (above the PBL). Precipitating particles increase in amount and start to fall to the ground, as indicated by the descending echo. As this initial cell moves away from the maximum low-level forcing, a new cell starts to form in a similar way. By 2016, this new cell reaches the stage of the first cell at 1956, so the period of new cell initiation is about 20 min in this case. This process repeats itself, creating a group of cells, emanating from maximum surface forcing and exhibiting the previously mentioned "plume" pattern of convection (cf. Fig. 9 of Part I) downwind (in the direction of midlevel winds), until the sustained lifting is interrupted by the cold pool (cf. Fig. 6 of Part I) created by these cells.

The sequence of vertical cross sections in Fig. 4 also shows clearly that the root or source of cell A is at the + point in Fig. 3a, instead of the location NE of + on the dry side of the surface convergence band. In other words, the "first echo" seen by radar is displaced by advection from the location where the cloud was initiated. Hane et al. (1997) presented evidence of moist air with clouds being carried eastward from a plume of moist air forced upward by the dryline convergence, using sounding and aircraft data, although in that case, the clouds did not develop into deep convection. The processes involved are, however, similar.

To isolate the possible effect of condensational heating associated with the cloud formation on the low-level forcing, we made a 1-km "dry" simulation that is identical to the control simulation except that the condensation process is turned off in the model. The plots corresponding to Figs. 4a–d are shown in Fig. 5. It is clear that the low-level moisture convergence and the associated updraft are the cause rather than result of the developing clouds, confirming the key role of the forcing by BL eddies and rolls.

For cell B, whose echo first appears at around 2015, cross sections through the cell center in the convergence-band-parallel (B1–B2) and normal (B3–B4) directions are shown in Figs. 6 and 7. The first cross section goes through a convergence maximum located about 7 km to the SW of the cell (marked by + in Fig. 3b), and the second reveals band-normal circulations. In the cross sections through B1–B2, the development and evolution of clouds and precipitation is similar to those along A1–A2. A broader zone (because B1–B2 goes through the center of the HCR band) of strong low-level convergence is centered at roughly 13 km from B1 and the first echo appears at 2015 at about 7 km downstream (to the NE along B1–B2). The broader convergence zone forces wider clouds, and as the old cell moves away from the forcing region, again along the convergence band, a new cell develops (Fig. 6d), which eventually establishes its separate identity (Fig. 6f).

In the band-normal cross section through the center of the reflectivity echo at 2015 (B3–B4 in Fig. 3b), we see cell B when it is moving into the plane at 2015 (Fig. 7c) and when it is moving out of the plane at 2030 (Fig. 7f). In these cross sections, the low-level circulations appear more two-dimensional, with flows converging toward the HCR band in the lowest ½- to 1-km layer and forcing strong ascent. The inflow from the moist air mass is deeper at about 1-km depth, and that on the dry side, resulting from the HCR downdraft, is shallower (about 0.5 km deep). There is also a slight asymmetry with the downdraft as it slants toward the band during descent. The westerly momentum it carries would explain this. Another strong HCR convergence band is evident to the west in these cross sections.

For cell C, we draw a cross section through the echo center at 2027 and through the maximum low-level convergence center to its west-southwest (Fig. 8), and another cross section in the band-normal direction through the convergence maximum (Fig. 9; cf. Fig. 3c). The development and evolution of clouds and reflectivity echoes in Fig. 8 confirms that cell C originates at the low-level convergence maximum on the HCR band

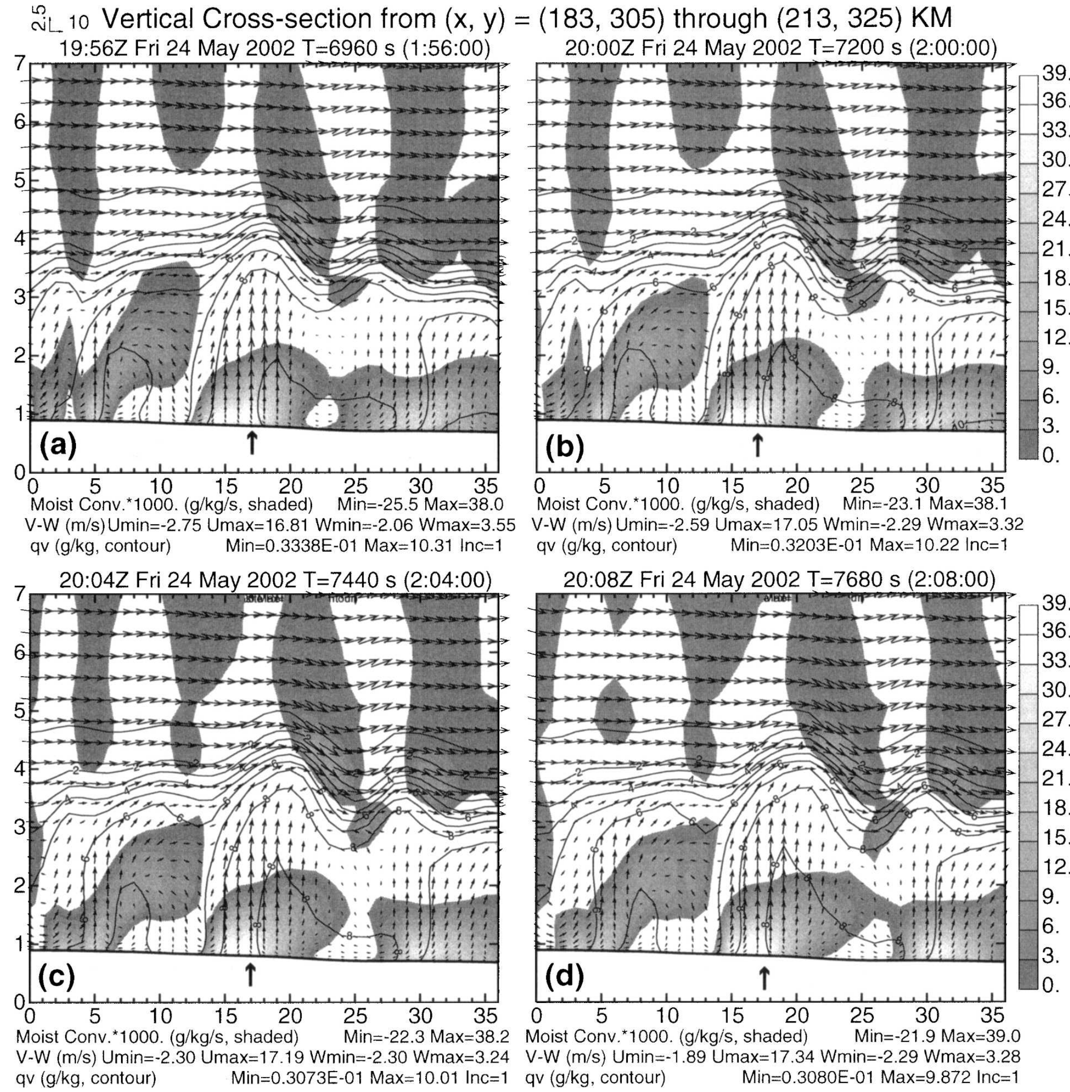


FIG. 5. As in Fig. 4 but for a corresponding dry run in which the condensation process is turned off. Shown are the times corresponding to the first four panels of Fig. 4.

(location + in Fig. 3c), even though its first echo appears about 5 km away from the band. The sustained forcing at the band and the development of new cells above the maximum forcing as older cells are advected away are more evident in this sequence of plots; in fact, during this 25-min period, three new cells developed. At 2037 (Fig. 8e), one decaying cell, one mature cell, and one new cell are present in the same plot. The period of cell regeneration is about 10 min in this case. Because the cross sections in Fig. 9 cut through the maximum low-level forcing, clouds are present at all times during this period; the left column shows newly created clouds and the right column shows developed clouds that are moving away from the strongest forcing.

The faster separation of the old cells from the convergence band associated with C is responsible for the shorter period, while the stronger midlevel advective flow is partly responsible for the faster separation. For example, the maximum horizontal wind along the cross sections in Fig. 8 for cell C is over 22 m s$^{-1}$ while that in Fig. 4 for cell A is about 18 m s$^{-1}$. The winds between the 3- and 4-km levels, where the initial clouds form, are about 15 m s$^{-1}$ in the former case, but are generally less than 10 m s$^{-1}$ for the latter.

The control on the period of cell regeneration by the strength of midlevel flow relative to the low-level forcing is believed to be similar to the cell regeneration process at the gust front of multicellular squall lines, as discussed by Lin and Joyce (2001) and Fovell and Tan (1998). Lin and Joyce (2001) show that the period of

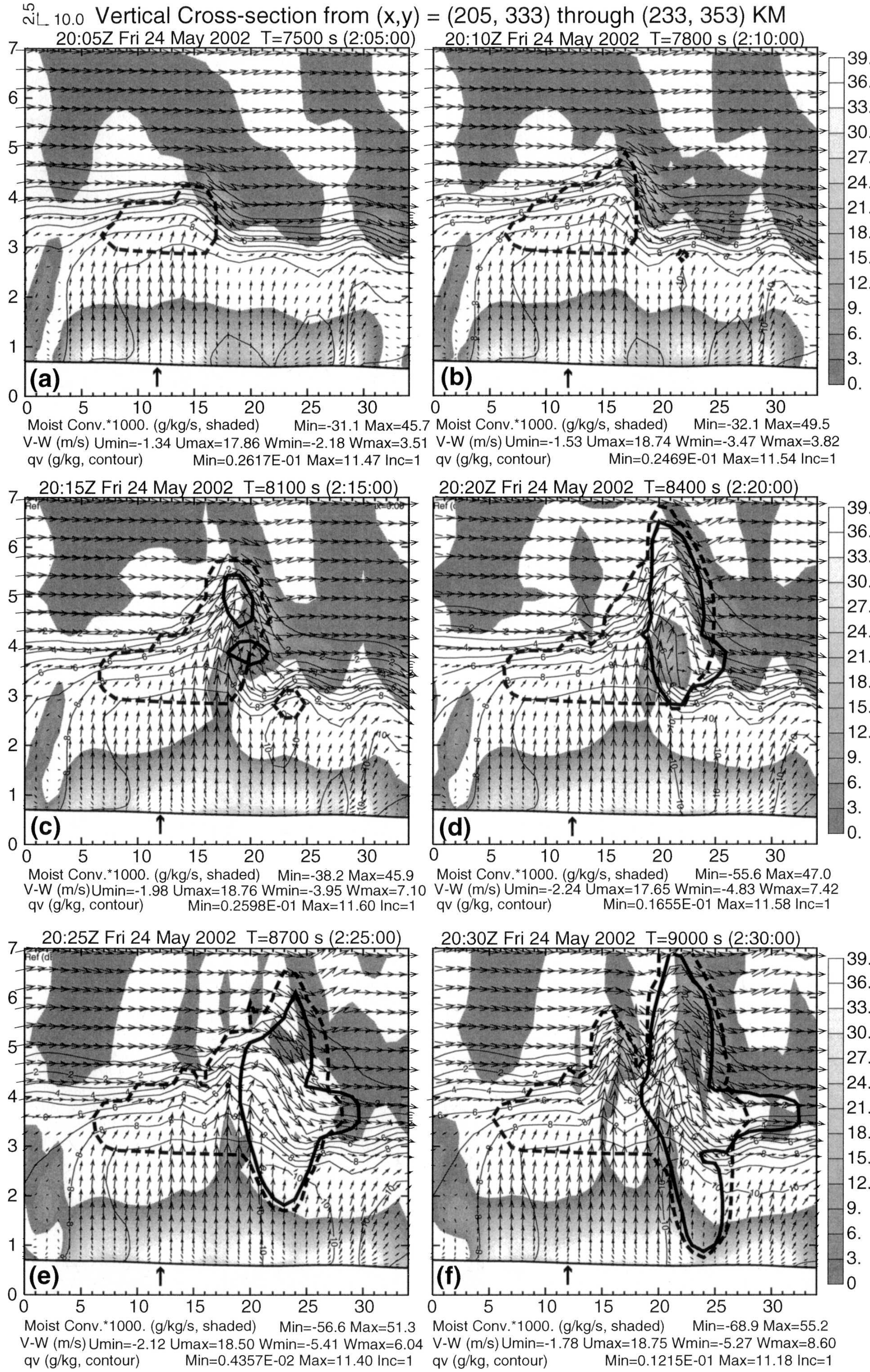


FIG. 6. As in Fig. 4, but for the vertical cross sections along line B1–B2 in Fig. 3b at 5-min intervals starting at 2005 UTC 24 May 2002: $t$ = (a) 7500 s, (b) 7800 s, (c) 8100 s, (d) 8400 s, (e) 8700 s, and (f) 9000 s. The origin is at B1.

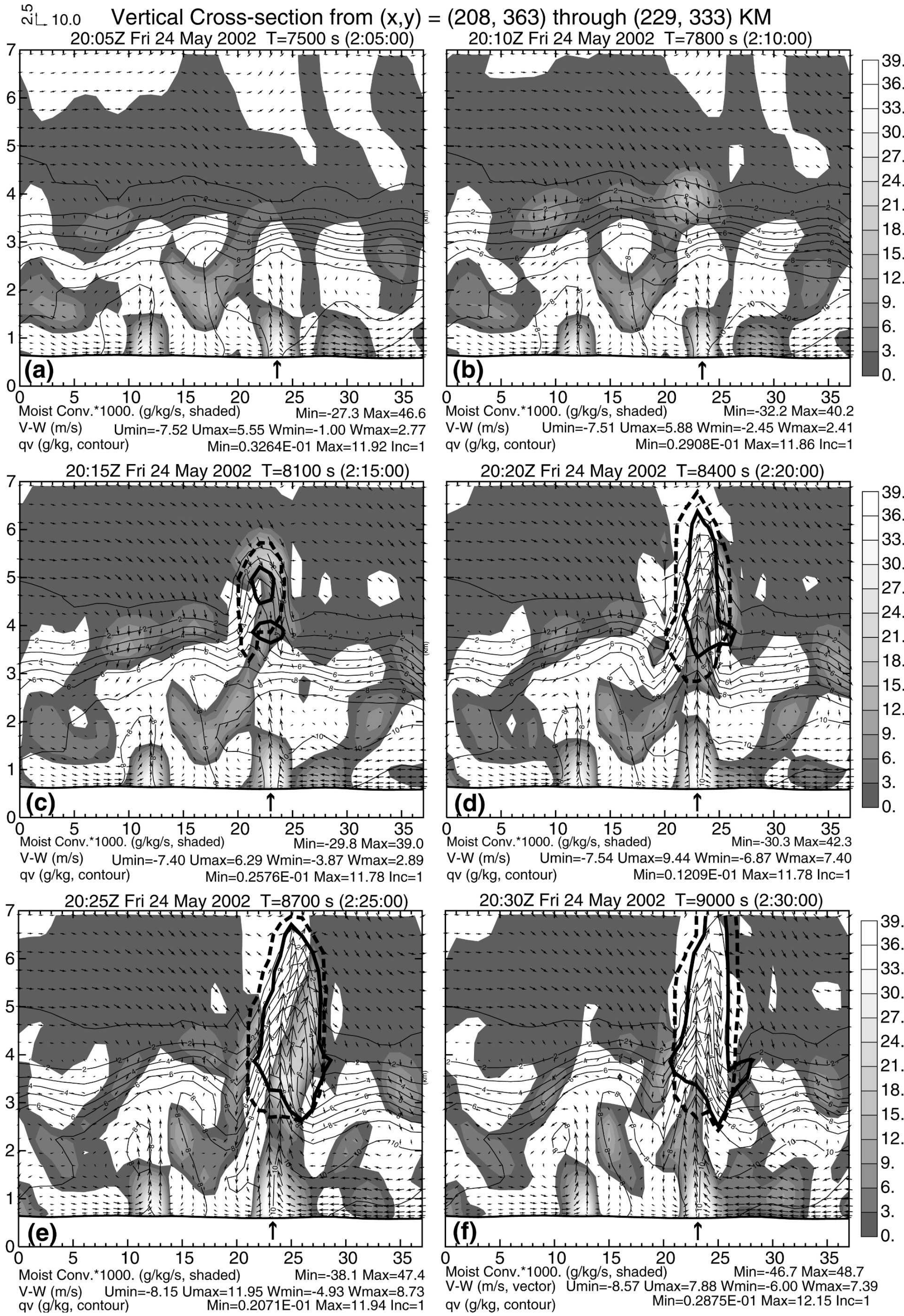


FIG. 7. As in Fig. 4, but for the vertical cross sections along line B3–B4 in Fig. 3b at 5-min intervals starting at 2005 UTC 24 May 2002: $t$ = (a) 7500 s, (b) 7800 s, (c) 8100 s, (d) 8400 s, (e) 8700 s, and (f) 9000 s. The origin is at B3.

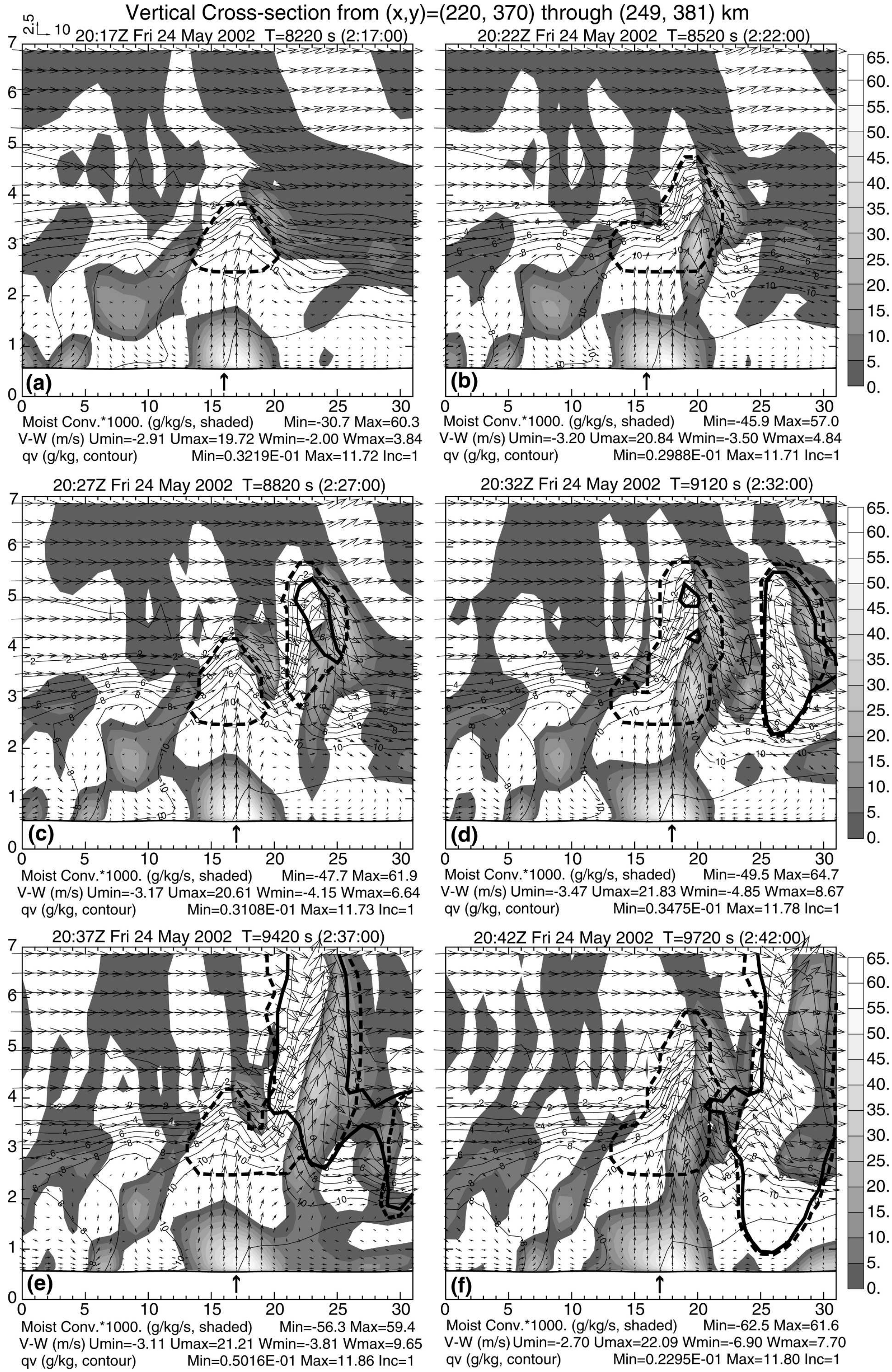


FIG. 8. As in Fig. 4, but for the vertical cross sections along line C1–C2 in Fig. 3c at 5-min intervals starting at 2017 UTC 24 May 2002: $t$ = (a) 8220 s, (b) 8520 s, (c) 8820 s, (d) 9120 s, (e) 9420 s, and (f) 9720 s. The origin is at C1.

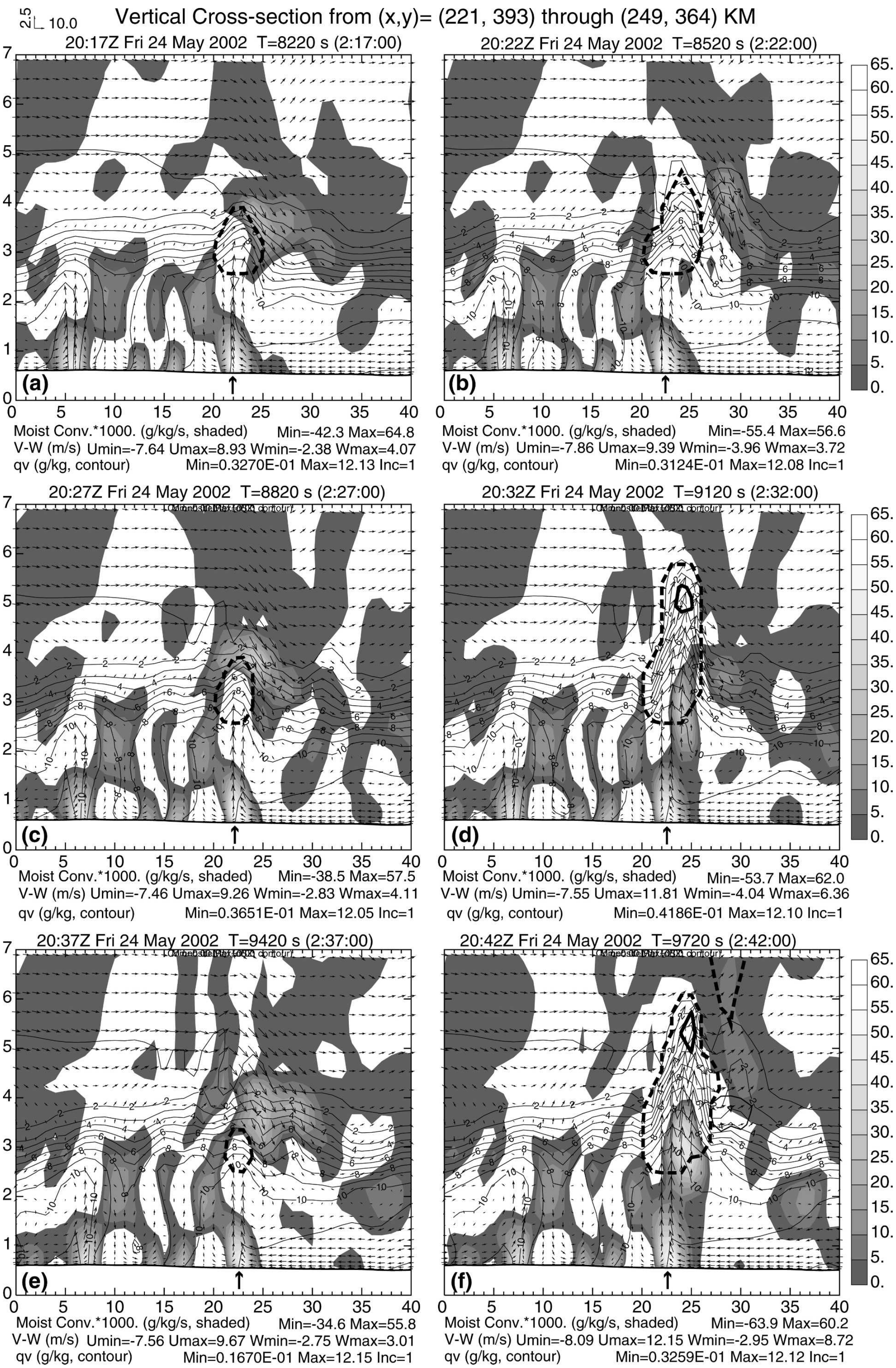


FIG. 9. As in Fig. 4, but for the vertical cross sections along line C3–C4 in Fig. 3c at 5-min intervals starting at 2017 UTC 24 May 2002: $t$ = (a) 8220 s, (b) 8520 s, (c) 8820 s, (d) 9120 s, (e) 9420 s, and (f) 9720 s. The origin is at C3.

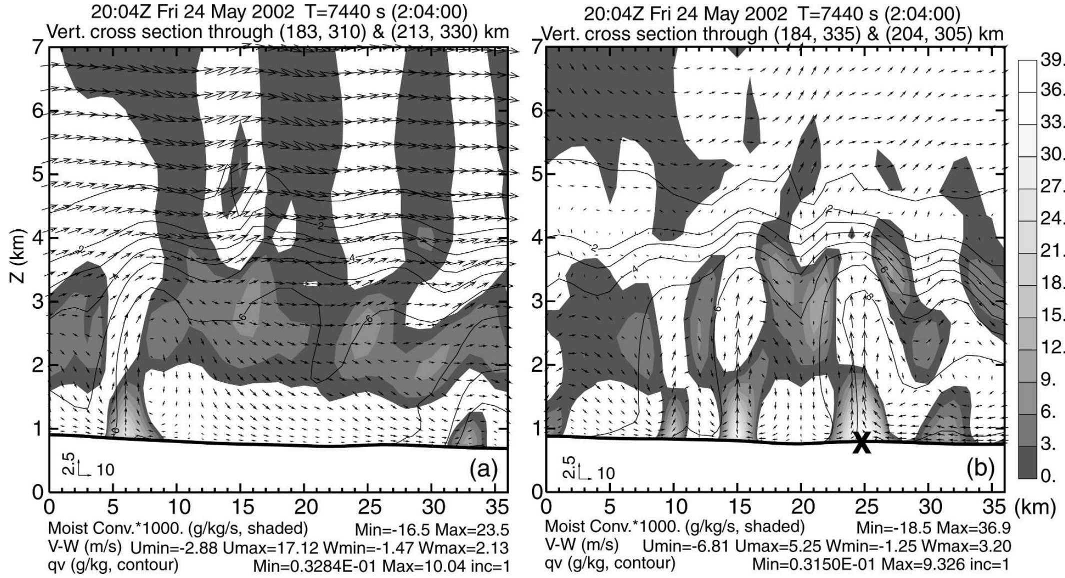


FIG. 10. The same fields as in Fig. 4, but for vertical cross section through (a) line A3–A4 and (b) line A5–A6 in Fig. 3a. The location of "x" in (b) corresponds to that of "+" in Fig. 3a.

cell regeneration is inversely proportional to the storm-relative midlevel inflow speed in the squall-line case. The influence of lower-tropospheric winds on the convective storm formation along drylines has also been studied by Peckham and Wicker (2000), using idealized numerical simulations. They found that a weaker cross-dryline lower-to-midtropospheric flow creates a more favorable condition for deep convective storms to develop, because, as one of the reasons, the lifted air parcels are able to remain above the low-level forcing for a longer period of time. In our case, the moderate midlevel flow is apparently not too strong to inhibit the intensification of initial storm cells.

Another fact worth noting is that the first cell in this group, that is, cell C, did not develop as intensely—it never reached above 6 km (Fig. 8)—while the first cells at the locations of A and B reached 7-km height in 12 to 15 min. The key difference is that cell C was advected away from the low-level convergence band, while cells A and B remained above the band throughout their growing stage. A further examination of the cloud water fields (not shown) reveals that the first cloud actually formed above the HCB near C earlier, at around 1930, than those near A (at 1950) and B (at 1957). This cloud propagated northeastward away from the HCB and dissipated after producing a tiny echo exceeding 20 dB*Z*. The cell we observe in the model developed out of the second cloud forming above the same region. The fact that clouds form earlier at the location of C agrees with satellite observations.

To further understand the structure of the boundary layer convective eddies that interact with the dryline, we plot in Fig. 10 additional vertical cross sections along the long (A3–A4 in Fig. 3a) and short (A5–A6 in Fig. 3a) axes of the elliptically shaded eddy immediately west of the initiation point of cell A. This eddy is responsible for creating convergence band R5 in Fig. 2. Figure 10 shows that this eddy is roughly 2 to 2.5 km deep. The prevailing wind above the boundary layer is from the southwest, which is also the orientation of the long axis and of the associated low-level convergence bands (the low-level vertical wind shear vector is also roughly in the same direction). The circulation along the long axis is clearly asymmetric, with the center of maximum downdraft located closer to the SW end of the axis (Fig. 10a). The downdraft NE of this center carries a significant amount of southwesterly momentum from the 3–4-km level down to the surface, implying a significant amount of downward momentum transport.

The cross section along the direction of short axis, or in the direction perpendicular to the low-level convergence bands, exhibits a more symmetric circulation pattern (Fig. 10b). This short axis is chosen to go through point + in Fig. 3a, the point of maximum forcing for cell A. The strong downdraft of more than 1 m $s^{-1}$ at the center of the eddy and resultant strong convergence on its eastern edge clearly contribute to the strong surface convergence at location "x" in Fig. 10b. Because of the rather symmetric vertical circulation, downward momentum transport does not seem to have played a direct role in enhancing surface convergence at x. It has, however, affected the location of the maximum surface convergence, by affecting the vertical circulation in the long-axis direction. Interestingly, despite the much enhanced southwesterly flow at the surface, the maximum surface convergence does not occur at the NE end of the eddy (or long axis), but at the SE edge of the eddy with a SW bias in location. The same is true for the eddy responsible for the triggering of cell B (Fig. 3b). The situation with cell C is different because the surface divergent flows are enhanced in the southeastward instead of northwestward direction (Fig. 3c), for reasons discussed in section 3a. As a result, the convergence in the HCB associated with C is stronger (Fig. 3), and clouds form earlier (not shown). The stronger band-normal cloud-level flow with C caused the first cloud to dissipate before cell C developed.

### c. *Role of misocyclones*

We have seen that the updrafts that force cells A, B, and C are not collocated with the centers of maximum vertical vorticity or misocyclones, and this is especially true for cell C. For cell C, the maximum forcing is located in between two well-defined misocyclones (marked as *V5* and *V6* in Fig. 3c) although it is closer to the northern one. The circulation of vortex *V6* should help enhance the convergence at the location of +, although it is clear that most of the convergence at this point is due to the opposing flows from the HCR divergence center marked as *D7* (Fig. 3c) and the southeasterly flow east of the PDCB. The center of vortex *V6* actually exhibits a convergence minimum. As mentioned in the introduction, misocyclones often contain dynamically induced downdraft at their core, which would reduce low-level convergence or create a divergence. Observational evidence of misocyclone downdrafts has been documented by Murphey et al. (2006) and Markowski and Hannon (2006) for two different IHOP_2002 cases.

Misocyclone *V5* does collocate with the low-level convergence maximum, however (Fig. 3c). We would again, however, attribute this convergence maximum to the strong divergence center, *D6*, located right to its west. This convergence maximum actually triggers a storm cell later on, after three cells are produced at the + point. We consider this to be a coincidence rather than suggesting that the misocyclone promotes updraft. It is not clear if the suggestion by Wilson et al. (1992) about misocyclones containing enhanced updraft is due to a similar coincidence or due to insufficient data resolution in separating a nearby updraft from the misocyclone center.

The situations with cells A and B are different from cell C but similar to each other. In both cases, the maximum surface lifting is located between a couplet of positive and negative vorticity centers found on their respective HCB. A careful examination of the time evolution of the fields shows that strong convergence created by the interaction of HCR and OCC divergent flows (e.g., *D1*, *D2*, and *D3,* the centers of divergence in Fig. 3a) and with the flow from east of the PDCB precedes the concentration of vorticity at these centers. The negative vorticity originates from the tilting of horizontal vorticity, while the positive vorticity comes from the same process as well as from existing vertical vorticity in the background. The updraft located between the vorticity couplets provides stretching and further tilting that increases the vorticity. In other words, the updraft or vertical lifting is the cause, not the result, of these vortices.

## 4. Conceptual model

Based on the analysis of our simulation results, supported by observational evidence reported by other authors on this and other cases, we propose in the following conceptual model of dryline convective initiation as related to the interaction of HCRs with the PDCB.

In this conceptual model (Fig. 11), HCRs develop on both sides of the dryline in the afternoon due to surface heating over sloping terrain. Close to the PDCB, which is located at the eastern edge of the zone of strong surface moisture gradient and between the generally southeasterly moist flow and the generally southwesterly drier flow, the HCRs are aligned at an acute angle, $\alpha$, with the dryline (see Fig. 11). The HCRs on the west side are more intense and deeper and their updraft speed can reach several meters per second. Often, HCRs cease to exist or significantly weaken east of the PDCB, due to suppression by a broad branch of descending motion that is part of the developing mesoscale dryline circulation. The HCRs west of PDCB are initially quasi-two-dimensional (Fig. 11a) but become more cellular with time (Fig. 11b). The low-level convergence bands associated with the HCR updrafts are shown by gray shading in the figure and are enhanced at the dryline location. The unperturbed PDCB (long, straight, short-dashed line in the figure) is the would-be location of the convergence boundary between the moist and dry air masses if the HCRs were absent. The convergence boundary when the HCRs are fully developed (thick solid line in Fig. 11b) is distorted into a wavy pattern by the intersecting HCRs (see Fig. 11b). This wavy pattern is often further enhanced by vorticity centers that form along the distorted PDCB.

As the dryline is strengthened in the afternoon, the easterly component of moist flow is increased. In the absence of other complications, convective initiation is

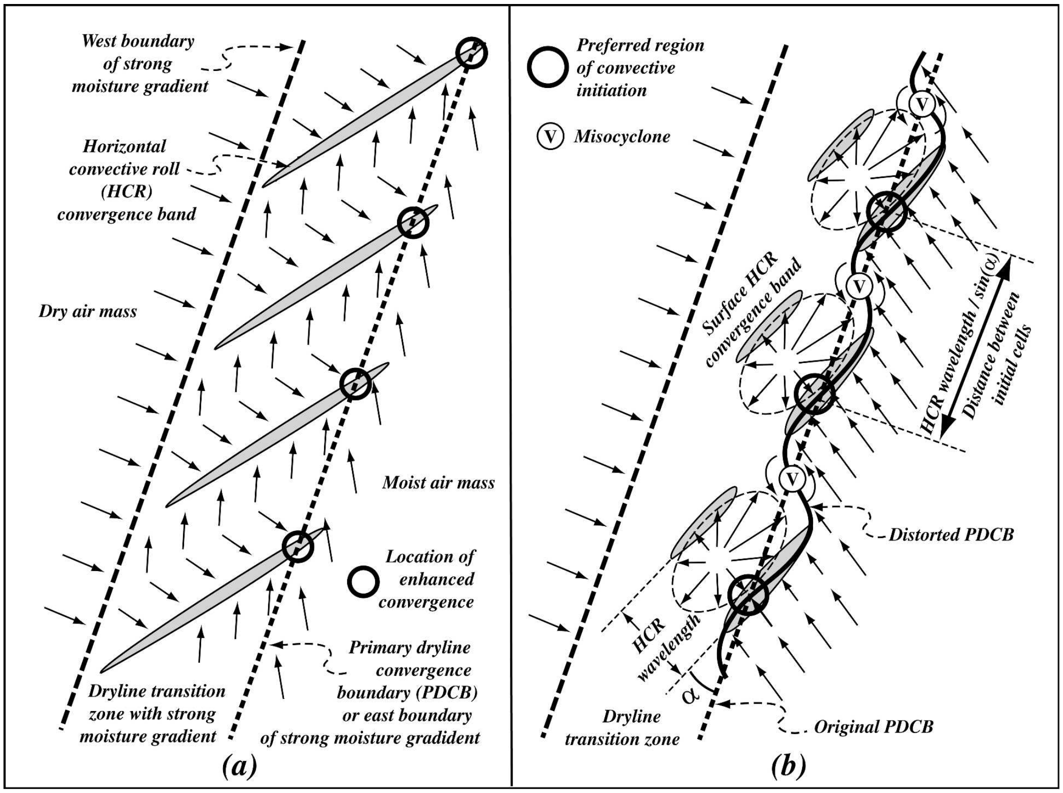


FIG. 11. A conceptual model of dryline convective initiation due to the interaction of the PDCB with the evolving HCRs that originate at and on the west side of the PDCB and are aligned at an acute angle, $\alpha$, with the dryline. The PDCB is the boundary between the southerly to southeasterly moist flow and the drier, generally westerly flow in the dryline transition zone, where a strong moist gradient is found. The PDCB undistorted by the HCR circulation is marked by the thick, straight, short-dashed line. The thick, straight, long-dashed line marks the location of the western boundary of the dryline transition zone, toward the west of which the air is exclusively from the dry high plateau to the west with a specific humidity of few g kg$^{-1}$. (a) The earlier stage of HCR development when the HCRs are quasi-two-dimensional and the roll circulations result in surface divergence flow and convergence bands (shaded gray) between the opposing roll circulations. The background southwesterly wind in the transition zone causes the surface divergence flow of the rolls to point in the downwind direction. The rolls are aligned in the direction of the mean low-level vertical shear vector and the northeastern ends of the convergence bands intersect the PDCB, creating localized convergence maxima. (b) The low-level flow at the mature stage of HCR development, about 1–2 h after (a), when significant cellular structures develop with the rolls and the convergence bands become segmented and shorter but more intense. The convergence bands protrude further into the moist air mass across the original PDCB and distort the PDCB into a wavy pattern. The divergence flow between the convergence bands develops into asymmetric elliptic patterns, with the northeastward wind components being stronger due to downward transport of southwesterly momentum and due to the original background flow in the same direction. The mesoscale convergence along the dryline is enhanced by the elevated heating to the west, hence by the increased solenoidal forcing. It narrows the dryline transition zone, turns the HCRs into a more north–south orientation. The easterly component of the moist flow is increased, which, together with HCR divergence flow, creates convergence maxima along the PDCB, at locations marked by thick circles, where convective initiation is preferred. Such locations are also roughly where HCRs intersect the original PDCB and the distance between such preferred locations is roughly equal to the HCR wavelength divided by sin($\alpha$). When the initiated clouds move along the HCR convergence bands, they develop into deeper clouds faster and have a much better chance of growing into a full intensity convective storm. When older cells that are initiated at the persistent maximum low-level convergence forcing move away, new cells tend to form at the same location, resulting in a series of cells. The thin circles enclosing "V" indicate locations of vorticity maxima (or misocyclones) along the PDCB. Misocyclones usually do not collocate with maximum surface convergence but their circulation can enhance convergence to their south and north, and nonsupercell tornadoes can develop when their vertical vorticity is stretched by cumulus congestus clouds that move over them.

preferred close to the central portion of the leading HCR convergence bands at the PDCB, where surface convergence is maximized due to opposing winds on each side of the bands as well as along-band flow convergence found at these locations. The three-dimensional aspect of the HCRs, due to the presence of cellular structures in the boundary layer convection, is responsible for the along-band convergence. These preferred locations are also the intercepting points of the leading HCRs with the otherwise unperturbed (straight) PDCB. As a result, the spacing between initial convective cells along the dryline tends to be equal to the distance between successive HCR updraft or near-surface convergence bands multiplied by $\sec(\alpha)$ (see Fig. 11b). The low-level environment has been preconditioned for easy triggering of convection along this zone because of sustained mesoscale lifting at the PDCB.

The general confluent flow pattern between the two air masses, and the significant local enhancement of westerly, southwesterly, or northwesterly winds by downward momentum transport due to intense BL eddies, are the primary sources for the enhancement and maintenance of the PDCB. The PDCB moves eastward during the day as a result of the intense vertical mixing to the west. Because of PDCB convergence, the top of the well-mixed moist layer is often half a kilometer or so higher in the PDCB region than that to the east, making the LFC easier to reach by individual parcels. The further lifting by HCR convergence pushes the air parcels above the LFC and triggers moist convection.

When the initial clouds that form above the localized maximum convergence forcing propagate, mainly due to advection, along the HCR convergence band, they growth faster and attain a higher intensity. In fact, the initial clouds that propagate away, due to band-normal midlevel flow, from the convergence band immediately after it forms often dissipate. Such clouds do help condition the environment, through moistening, for later deeper clouds to develop.

Behind the leading convergence bands are elliptically shaped asymmetric surface divergence patterns with the asymmetry arising from the fact that the air feeding the downdrafts already possesses westerly, southwesterly, and sometimes northwesterly momentum. The surface divergence patterns give rise to convergence maxima near the center of the bands. The convergence at the (usually northeast) end of the long axis of an ellipse is weaker because the flow ahead of it is generally from the southeast, which gives rise to strong directional shear. Vertical vorticity centers are found at such locations (marked by circled Vs in the figure) and the centers may appear in pairs, with each located at the end of the two neighboring HCR convergence bands (see, e.g., Fig. 2d).

The background positive vertical vorticity present in the cross-dryline shear zone, and the horizontal vorticity tilted into the vertical by the HCR convergence-band updraft, are the main sources of vorticity found in the vorticity centers (or misocyclones) along the wavy convergence boundary. The tilting would create both positive and negative vorticity; therefore negative vorticity centers are also found, though less often and weaker. Both the advection by the cellular component of the HCRs and that by the self-induced flow are responsible for the concentration of vorticity into the centers. The latter mechanism is responsible for the Kelvin–Helmholtz instability associated with a shear zone.

Maximum updrafts usually do not collocate with the centers of maximum vorticity, or misocyclones. In fact, upward motion is usually decreased and downdrafts can even form at the core of misocyclones due to a dynamically induced downward pressure gradient force at the low levels. Maximum updrafts usually exist to the north or south of the misocyclones, or in between them, where the convergence can be enhanced by the vortex circulations and initiation of convection is preferred.

## 5. Summary

In this paper, the output from a successful high-resolution numerical simulation of the 24 May 2002 dryline convective initiation (CI) case observed during IHOP_2002 is further analyzed. In particular, the structure and evolution of boundary layer convective eddies and horizontal rolls in the hours preceding the dryline convective initiation are carefully documented. The processes by which individual cells of moist convection are triggered are also analyzed in detail.

Horizontal convective rolls (HCRs) with aspect ratios (the ratio of roll spacing to depth) between 3 and 7 develop in the model on both sides of the dryline, with those on the west side being more intense and their updrafts reaching several meters per second. The main HCRs that interact with the primary dryline convergence boundary (PDCB) are those from the west side, and they are aligned at an acute angle with the dryline. They intercept the PDCB and create strong moisture convergence bands at the surface and force the PDCB into a wavy pattern. The downdrafts of HCRs and the associated surface divergence play a critical role in creating localized maxima of surface convergence that trigger convection. The downward transport of westerly or southwesterly momentum by the HCR downdrafts creates asymmetric surface divergence patterns that modulate the exact location of maximum convergence.

Sequences of convective cells develop at the centers of persistent maximum surface convergence, then move away from the source with the midlevel winds. While the mesoscale convergence of dryline circulation preconditions the boundary layer by deepening the mixed layer and lifting moist air parcels to their LCL, it is the localized forcing by the HCR circulation that provides the extra lifting for air parcels to rise above their LFC at specific locations along the line; deep moist convection subsequently develops at these locations. The maximum low-level forcing usually does not collocate with the centers of maximum vorticity; therefore, misocyclones usually do not trigger convection. A conceptual model summarizing these findings is proposed.

*Acknowledgments.* This work was primarily supported by NSF Grant ATM0129892. The first author was also supported by NSF ATM-9909007, ATM-0331594, and EEC-0313747, a DOT-FAA grant via DOC-NOAA NA17RJ1227, a grant from the Chinese Natural Science Foundation (40028504), and the "Outstanding Overseas Scholars" Award of Chinese Academy of Sciences (Grant 2004-2-7). Geoffrey Stano is acknowledged for some initial data preparation. Assistance was also provided by Keith Brewster. A Linux cluster operated by OSCER of University of Oklahoma and the NSF-supported Terascale Computing System at the Pittsburgh Supercomputing Center was used for the simulations. We thank Carl Hane for carefully reviewing the manuscript. The comments of three anonymous reviewers also improved the paper.

## REFERENCES

Agee, E. M., T. S. Chen, and K. E. Doswell, 1973: A review of mesoscale cellular convection. *Bull. Amer. Meteor. Soc.,* **54,** 1004–1012.

Atkins, N. T., R. M. Wakimoto, and C. L. Ziegler, 1998: Observations of the finescale structure of a dryline during VORTEX 95. *Mon. Wea. Rev.,* **126,** 525–550.

Balaji, V., and T. L. Clark, 1988: Scale selection in locally forced convective fields and the initiation of deep cumulus. *J. Atmos. Sci.,* **45,** 3188–3211.

Batchelor, G. K., 1967: *An Introduction to Fluid Dynamics*. Cambridge University Press, 615 pp.

Bluestein, H. B., and S. S. Parker, 1993: Modes of isolated, severe convective storm formation along the dryline. *Mon. Wea. Rev.,* **121,** 1352–1374.

Buban, M. S., C. L. Ziegler, and E. N. Rasmussen, 2003: The kinetic and thermodynamic effects of vortices within a dryline. Preprints, *31th Conf. on Radar Meteorology*, Seattle, WA, Amer. Meteor. Soc., 789–792.

Crook, N. A., M. W. Moncrieff, and T. L. Clark, 1991: The Denver cyclone. Part II: Interaction with the convective boundary layer. *J. Atmos. Sci.,* **48,** 2109–2126.

Fovell, R. G., and P.-H. Tan, 1998: The temporal behavior of numerically simulated multicell-type storms. Part II: The convective cell life cycle and cell regeneration. *Mon. Wea. Rev.,* **126,** 551–577.

Fujita, T. T., 1981: Tornadoes and downbursts in the context of generalized planetary scales. *J. Atmos. Sci.,* **38,** 1511–1534.

Geerts, B., R. Damiani, and S. Haimov, 2006: Finescale vertical structure of a cold front as revealed by airbone Doppler radar. *Mon. Wea. Rev.,* **134,** 251–271.

Hane, C. E., and H. Richter, 2004: On the importance of processes in the dry air upon convective initiation along the dryline. Preprints, *22d Conf. on Severe Local Storms*, Hyannis, MA, Amer. Meteor. Soc., CD-ROM, 10.1.

——, C. L. Ziegler, and H. B. Bluestein, 1993: Investigation of the dryline and convective storms initiated along the dryline: Field experiments during COPS-91. *Bull. Amer. Meteor. Soc.,* **74,** 2133–2145.

——, H. B. Bluestein, T. M. Crawford, M. E. Baldwin, and R. M. Rabin, 1997: Severe thunderstorm development in relation to along-dryline variability: A case study. *Mon. Wea. Rev.,* **125,** 231–251.

——, M. E. Baldwin, H. B. Bluestein, T. M. Crawford, and R. M. Rabin, 2001: A case study of severe storm development along a dryline within a synoptically active environment. Part I: Dryline motion and an Eta Model forecast. *Mon. Wea. Rev.,* **129,** 2183–2204.

——, R. M. Rabin, T. M. Crawford, H. B. Bluestein, and M. E. Baldwin, 2002: A case study of severe storm development along a dryline within a synoptically active environment. Part II: Multiple boundaries and convective initiation. *Mon. Wea. Rev.,* **130,** 900–920.

Holt, T. R., D. Niyogi, F. Chen, K. Manning, M. A. LeMone, and A. Qureshi, 2006: Effect of land–atmosphere interactions on the IHOP 24–25 May 2002 convection case. *Mon. Wea. Rev.,* **134,** 113–133.

Klemp, J. B., and R. Rotunno, 1983: A study of the tornadic region within a supercell thunderstorm. *J. Atmos. Sci.,* **40,** 359–377.

Kristovich, D. A. R., N. F. Laird, M. R. Hjelmfelt, R. G. Derickson, and K. A. Cooper, 1999: Transitions in boundary layer meso-convective structures: An observational case study. *Mon. Wea. Rev.,* **127,** 2895–2909.

Lane, T. P., and T. L. Clark, 2002: Gravity waves generated by the dry convective boundary layer: Two-dimensional scale selection and boundary-layer feedback. *Quart. J. Roy. Meteor. Soc.,* **128,** 1543–1570.

Lee, B. D., and R. B. Wilhelmson, 1997: The numerical simulation of non-supercell tornadogenesis. Part I: Initiation and evolution of pretornadic misocyclone circulations along a dry outflow boundary. *J. Atmos. Sci.,* **54,** 32–60.

LeMone, M. A., 1990: Some observations of vertical velocity skewness in the convective planetary boundary layer. *J. Atmos. Sci.,* **47,** 1163–1169.

Lin, Y.-L., and L. E. Joyce, 2001: A further study of the mechanisms of cell regeneration, propagation, and development within two-dimensional multicell storms. *J. Atmos. Sci.,* **58,** 2957–2988.

Markowski, P., and C. Hannon, 2006: Multiple-Doppler radar observations of the evolution of vorticity extrema in a convective boundary layer. *Mon. Wea. Rev.,* **134,** 355–374.

Mueller, C. K., and R. E. Carbone, 1987: Dynamics of a thunderstorm outflow. *J. Atmos. Sci.,* **44,** 1879–1898.

Murphey, H. V., R. M. Wakimoto, C. Flamant, and D. E. Kingsmill, 2006: Dryline on 19 June 2002 during IHOP. Part I: Airborne Doppler and LEANDRE II analyses of the thin line structure and convection initiation. *Mon. Wea. Rev.,* **134,** 406–430.

Peckham, S. E., and L. J. Wicker, 2000: The influence of topography and lower-tropospheric winds on dryline morphology. *Mon. Wea. Rev.,* **128,** 2165–2189.

——, R. B. Wilhelmson, L. J. Wicker, and C. L. Ziegler, 2004: Numerical simulation of the interaction between the dryline and horizontal convective rolls. *Mon. Wea. Rev.,* **132,** 1792–1812.

Rao, P. A., and H. E. Fuelberg, 2000: An investigation of convection behind the Cape Canaveral sea-breeze front. *Mon. Wea. Rev.,* **128,** 3437–3458.

Rhea, J. O., 1966: A study of thunderstorm formation along drylines. *J. Appl. Meteor.,* **5,** 58–63.

Richardson, Y. P., J. W. Wurman, and C. Hartman, 2003: Multi-Doppler analysis of convective initiation on 19 June 2002 during IHOP_2002. Preprints, *31th Conf. on Radar Meteorology*, Seattle, WA, Amer. Meteor. Soc., CD-ROM, 11A.6.

Richter, H., and C. E. Hane, 2003: On the convective "ignition" of potentially unstable boundary layers over land. Bureau of Meteorology Research Centre Modeling Workshop, BMRC Res. Rep. 93, 79–84.

Shaw, B. L., R. A. Pielke, and C. L. Ziegler, 1997: A three-dimensional numerical simulation of a Great Plains dryline. *Mon. Wea. Rev.,* **125,** 1489–1506.

Wakimoto, R. M., and J. W. Wilson, 1989: Nonsupercell tornadoes. *Mon. Wea. Rev.,* **117,** 1113–1140.

——, H. V. Murphey, E. V. Browell, and S. Ismail, 2006: The "triple/point" on 24 May 2002 during IHOP: Part I: Airborne Doppler and LASE analyses of the frontal boundaries and convection initiation. *Mon. Wea. Rev.,* **134,** 231–250.

Weckwerth, T. M., J. W. Wilson, R. M. Wakimoto, and N. A. Crook, 1997: Horizontal convective rolls: Determining the environmental conditions supporting their existence and characteristics. *Mon. Wea. Rev.,* **125,** 505–526.

——, and Coauthors, 2004: An overview of the International $H_2O$ Project (IHOP_2002) and some preliminary highlights. *Bull. Amer. Meteor. Soc.,* **85,** 253–277.

Wilson, J. W., G. B. Foote, N. A. Crook, J. C. Fankhauser, C. G. Wade, J. D. Tuttle, C. K. Mueller, and S. K. Krueger, 1992: The role of boundary-layer convergence zones and horizontal rolls in the initiation of thunderstorms: A case study. *Mon. Wea. Rev.,* **120,** 1785–1815.

Xue, M., and W. Martin, 2006: A high-resolution modeling study of the 24 May 2002 dryline case during IHOP. Part I: Numerical simulation and general evolution of the dryline and convection. *Mon. Wea. Rev.,* **134,** 149–171.

——, K. K. Droegemeier, and V. Wong, 2000: The Advanced Regional Prediction System (ARPS)—A multiscale nonhydrostatic atmospheric simulation and prediction tool. Part I: Model dynamics and verification. *Meteor. Atmos. Phys.,* **75,** 161–193.

——, D.-H. Wang, J.-D. Gao, K. Brewster, and K. K. Droegemeier, 2003: The Advanced Regional Prediction System (ARPS), storm-scale numerical weather prediction and data assimilation. *Meteor. Atmos. Phys.,* **82,** 139–170.

Ziegler, C. L., and C. E. Hane, 1993: An observational study of the dryline. *Mon. Wea. Rev.,* **121,** 1134–1151.

——, and E. N. Rasmussen, 1998: The initiation of moist convection at the dryline: Forecasting issues from a case study perspective. *Wea. Forecasting,* **13,** 1106–1131.

——, W. J. Martin, R. A. Pielke, and R. L. Walko, 1995: A modeling study of the dryline. *J. Atmos. Sci.,* **52,** 263–285.

——, T. J. Lee, and R. A. Pielke Sr., 1997: Convective initiation at the dryline: A modeling study. *Mon. Wea. Rev.,* **125,** 1001–1026.